

AperTO - Archivio Istituzionale Open Access dell'Università di Torino

Measurement of the average shape of longitudinal profiles of cosmic-ray air showers at the Pierre Auger Observatory

This is a pre print version of the following article:

Original Citation:

Availability:

This version is available <http://hdl.handle.net/2318/1699646> since 2019-04-20T16:05:34Z

Published version:

DOI:10.1088/1475-7516/2019/03/018

Terms of use:

Open Access

Anyone can freely access the full text of works made available as "Open Access". Works made available under a Creative Commons license can be used according to the terms and conditions of said license. Use of all other works requires consent of the right holder (author or publisher) if not exempted from copyright protection by the applicable law.

(Article begins on next page)

Measurement of the average shape of longitudinal profiles of cosmic-ray air showers at the Pierre Auger Observatory

A. Aab,⁷⁵ P. Abreu,⁶⁷ M. Aglietta,^{50,49} I.F.M. Albuquerque,¹⁹
J.M. Albury,¹² I. Allekotte,¹ A. Almela,^{8,11} J. Alvarez Castillo,⁶³
J. Alvarez-Muñiz,⁷⁴ G.A. Anastasi,^{42,43} L. Anchordoqui,⁸²
B. Andrada,⁸ S. Andringa,⁶⁷ C. Aramo,⁴⁷ H. Asorey,^{1,28}
P. Assis,⁶⁷ G. Avila,^{9,10} A.M. Badescu,⁷⁰ A. Bakalova,³⁰
A. Balaceanu,⁶⁸ F. Barbato,^{56,47} R.J. Barreira Luz,⁶⁷ S. Baur,³⁷
K.H. Becker,³⁵ J.A. Bellido,¹² C. Berat,³⁴ M.E. Bertaina,^{58,49}
X. Bertou,¹ P.L. Biermann,^b J. Biteau,³² S.G. Blaess,¹²
A. Blanco,⁶⁷ J. Blazek,³⁰ C. Bleve,^{52,45} M. Boháčová,³⁰
D. Boncioli,^{42,43} C. Bonifazi,²⁴ N. Borodai,⁶⁴ A.M. Botti,^{8,37}
J. Brack,^e T. Bretz,³⁹ A. Bridgeman,³⁶ F.L. Briechle,³⁹
P. Buchholz,⁴¹ A. Bueno,⁷³ S. Buitink,¹⁴ M. Buscemi,^{54,44}
K.S. Caballero-Mora,⁶² L. Caccianiga,⁵⁵ L. Calcagni,⁴
A. Cancio,^{11,8} F. Canfora,^{75,77} J.M. Carceller,⁷³ R. Caruso,^{54,44}
A. Castellina,^{50,49} F. Catalani,¹⁷ G. Cataldi,⁴⁵ L. Cazon,⁶⁷
J.A. Chinellato,²⁰ J. Chudoba,³⁰ L. Chytka,³¹ R.W. Clay,¹²
A.C. Cobos Cerutti,⁷ R. Colalillo,^{56,47} A. Coleman,⁸⁶
M.R. Coluccia,^{52,45} R. Conceição,⁶⁷ A. Condorelli,^{42,43}
G. Consolati,^{46,51} F. Contreras,^{9,10} M.J. Cooper,¹² S. Coutu,⁸⁶
C.E. Covault,⁸⁰ B. Daniel,²⁰ S. Dasso,^{5,3} K. Daumiller,³⁷
B.R. Dawson,¹² J.A. Day,¹² R.M. de Almeida,²⁶ S.J. de Jong,^{75,77}
G. De Mauro,^{75,77} J.R.T. de Mello Neto,^{24,25} I. De Mitri,^{42,43}
J. de Oliveira,²⁶ F.O. de Oliveira Salles,¹⁵ V. de Souza,¹⁸
J. Debatin,³⁶ O. Deligny,³² N. Dhital,⁶⁴ M.L. Díaz Castro,²⁰
F. Diogo,⁶⁷ C. Dobrigkeit,²⁰ J.C. D'Olivo,⁶³ Q. Dorosti,⁴¹
R.C. dos Anjos,²³ M.T. Dova,⁴ A. Dundovic,⁴⁰ J. Ebr,³⁰
R. Engel,^{36,37} M. Erdmann,³⁹ C.O. Escobar,^c A. Etchegoyen,^{8,11}
H. Falcke,^{75,78,77} J. Farmer,⁸⁷ G. Farrar,⁸⁵ A.C. Fauth,²⁰

N. Fazzini,^c F. Feldbusch,³⁸ F. Fenu,^{58,49} L.P. Ferreyro,⁸
J.M. Figueira,⁸ A. Filipčić,^{72,71} M.M. Freire,⁶ T. Fujii,^{87,f}
A. Fuster,^{8,11} B. García,⁷ H. Gemmeke,³⁸ A. Gherghel-Lascu,⁶⁸
P.L. Ghia,³² U. Giaccari,¹⁵ M. Giammarchi,⁴⁶ M. Giller,⁶⁵
D. Głás,⁶⁶ J. Glombitza,³⁹ G. Golup,¹ M. Gómez Berisso,¹
P.F. Gómez Vitale,^{9,10} N. González,⁸ I. Goos,^{1,37} D. Góra,⁶⁴
A. Gorgi,^{50,49} M. Gottowik,³⁵ T.D. Grubb,¹² F. Guarino,^{56,47}
G.P. Guedes,²¹ E. Guido,^{49,58} R. Halliday,⁸⁰ M.R. Hampel,⁸
P. Hansen,⁴ D. Harari,¹ T.A. Harrison,¹² V.M. Harvey,¹²
A. Haungs,³⁷ T. Hebbeker,³⁹ D. Heck,³⁷ P. Heimann,⁴¹
G.C. Hill,¹² C. Hojvat,^c E.M. Holt,^{36,8} P. Homola,⁶⁴
J.R. Hörandel,^{75,77} P. Horvath,³¹ M. Hrabovský,³¹ T. Huege,^{37,14}
J. Hulsman,^{8,37} A. Insolia,^{54,44} P.G. Isar,⁶⁹ I. Jandt,³⁵
J.A. Johnsen,⁸¹ M. Josebachuili,⁸ J. Jurysek,³⁰ A. Kääpä,³⁵
K.H. Kampert,³⁵ B. Keilhauer,³⁷ N. Kemmerich,¹⁹ J. Kemp,³⁹
H.O. Klages,³⁷ M. Kleifges,³⁸ J. Kleinfeller,⁹ R. Krause,³⁹
D. Kuempel,³⁵ G. Kukec Mezek,⁷¹ A. Kuotb Awad,³⁶
B.L. Lago,¹⁶ D. LaHurd,⁸⁰ R.G. Lang,¹⁸ R. Legumina,⁶⁵
M.A. Leigui de Oliveira,²² V. Lenok,³⁷ A. Letessier-Selvon,³³
I. Lhenry-Yvon,³² O.C. Lippmann,¹⁵ D. Lo Presti,^{54,44} L. Lopes,⁶⁷
R. López,⁵⁹ A. López Casado,⁷⁴ R. Lorek,⁸⁰ Q. Luce,³²
A. Lucero,⁸ M. Malacari,⁸⁷ G. Mancarella,^{52,45} D. Mandat,³⁰
B.C. Manning,¹² P. Mantsch,^c A.G. Mariazzi,⁴ I.C. Mariş,¹³
G. Marsella,^{52,45} D. Martello,^{52,45} H. Martinez,⁶⁰ O. Martínez
Bravo,⁵⁹ M. Mastrodicasa,^{53,43} H.J. Mathes,³⁷ S. Mathys,³⁵
J. Matthews,⁸³ G. Matthiae,^{57,48} E. Mayotte,³⁵ P.O. Mazur,^c
G. Medina-Tanco,⁶³ D. Melo,⁸ A. Menshikov,³⁸
K.-D. Merenda,⁸¹ S. Michal,³¹ M.I. Micheletti,⁶ L. Middendorf,³⁹
L. Miramonti,^{55,46} B. Mitrica,⁶⁸ D. Mockler,³⁶ S. Mollerach,¹
F. Montanet,³⁴ C. Morello,^{50,49} G. Morlino,^{42,43} M. Mostafá,⁸⁶
A.L. Müller,^{8,37} M.A. Muller,^{20,d} S. Müller,^{36,8} R. Mussa,⁴⁹
L. Nellen,⁶³ P.H. Nguyen,¹² M. Niculescu-Oglinzanu,⁶⁸
M. Niechciol,⁴¹ D. Nitz,^{84,g} D. Nosek,²⁹ V. Novotny,²⁹
L. Nožka,³¹ A. Nucita,^{52,45} L.A. Núñez,²⁸ A. Olinto,⁸⁷
M. Palatka,³⁰ J. Pallotta,² M.P. Panetta,^{52,45} P. Papenbreer,³⁵
G. Parente,⁷⁴ A. Parra,⁵⁹ M. Pech,³⁰ F. Pedreira,⁷⁴ J. Pękala,⁶⁴
R. Pelayo,⁶¹ J. Peña-Rodríguez,²⁸ L.A.S. Pereira,²⁰ M. Perlin,⁸
L. Perrone,^{52,45} C. Peters,³⁹ S. Petrera,^{42,43} J. Phuntsok,⁸⁶
T. Pierog,³⁷ M. Pimenta,⁶⁷ V. Pirronello,^{54,44} M. Platino,⁸

J. Poh,⁸⁷ B. Pont,⁷⁵ C. Porowski,⁶⁴ R.R. Prado,¹⁸ P. Privitera,⁸⁷
 M. Prouza,³⁰ A. Puyleart,⁸⁴ S. Querchfeld,³⁵ S. Quinn,⁸⁰
 R. Ramos-Pollan,²⁸ J. Rautenberg,³⁵ D. Ravignani,⁸
 M. Reininghaus,³⁷ J. Ridky,³⁰ F. Riehn,⁶⁷ M. Risse,⁴¹ P. Ristori,²
 V. Rizi,^{53,43} W. Rodrigues de Carvalho,¹⁹ J. Rodriguez Rojo,⁹
 M.J. Roncoroni,⁸ M. Roth,³⁷ E. Roulet,¹ A.C. Rovero,⁵
 P. Ruehl,⁴¹ S.J. Saffi,¹² A. Saftoiu,⁶⁸ F. Salamida,^{53,43}
 H. Salazar,⁵⁹ A. Saleh,⁷¹ G. Salina,⁴⁸ J.D. Sanabria Gomez,²⁸
 F. Sánchez,⁸ E.M. Santos,¹⁹ E. Santos,³⁰ F. Sarazin,⁸¹
 R. Sarmiento,⁶⁷ C. Sarmiento-Cano,⁸ R. Sato,⁹ P. Savina,^{52,45}
 M. Schauer,³⁵ V. Scherini,⁴⁵ H. Schieler,³⁷ M. Schimassek,³⁶
 M. Schimp,³⁵ F. Schlüter,³⁷ D. Schmidt,³⁶ O. Scholten,^{76,14}
 P. Schovánek,³⁰ F.G. Schröder,^{88,37} S. Schröder,³⁵
 J. Schumacher,³⁹ S.J. Sciutto,⁴ M. Scornavacche,⁸
 R.C. Shellard,¹⁵ G. Sigl,⁴⁰ G. Silli,^{8,37} O. Sima,^{68,h} R. Šmída,⁸⁷
 G.R. Snow,⁸⁹ P. Sommers,⁸⁶ J.F. Soriano,⁸² J. Souchard,³⁴
 R. Squartini,⁹ D. Stanca,⁶⁸ S. Stanič,⁷¹ J. Stasielak,⁶⁴ P. Stassi,³⁴
 M. Stolpovskiy,³⁴ A. Streich,³⁶ F. Suarez,^{8,11} M. Suárez-Durán,²⁸
 T. Sudholz,¹² T. Suomijärvi,³² A.D. Supanitsky,⁸ J. Šupík,³¹
 Z. Szadkowski,⁶⁶ A. Taboada,³⁷ O.A. Taborda,¹ A. Tapia,²⁷
 C. Timmermans,^{77,75} C.J. Toderó Peixoto,¹⁷ B. Tomé,⁶⁷
 G. Torralba Elipe,⁷⁴ P. Travnicek,³⁰ M. Trini,⁷¹ M. Tueros,⁴
 R. Ulrich,³⁷ M. Unger,³⁷ M. Urban,³⁹ J.F. Valdés Galicia,⁶³
 I. Valiño,^{42,43} L. Valore,^{56,47} P. van Bodegom,¹² A.M. van den
 Berg,⁷⁶ A. van Vliet,⁷⁵ E. Varela,⁵⁹ B. Vargas Cárdenas,⁶³
 R.A. Vázquez,⁷⁴ D. Veberič,³⁷ C. Ventura,²⁵ I.D. Vergara
 Quispe,⁴ V. Verzi,⁴⁸ J. Vicha,³⁰ L. Villaseñor,⁵⁹ J. Vink,⁷⁹
 S. Vorobiov,⁷¹ H. Wahlberg,⁴ A.A. Watson,^a M. Weber,³⁸
 A. Weindl,³⁷ M. Wiedeński,⁶⁶ L. Wiencke,⁸¹ H. Wilczyński,⁶⁴
 T. Winchen,¹³ M. Wirtz,³⁹ D. Wittkowski,³⁵ B. Wundheiler,⁸
 L. Yang,⁷¹ A. Yushkov,³⁰ E. Zas,⁷⁴ D. Zavrtnik,^{71,72}
 M. Zavrtnik,^{72,71} L. Zehrer,⁷¹ A. Zepeda,⁶⁰ B. Zimmermann,³⁷
 M. Ziolkowski,⁴¹ Z. Zong,³² and F. Zuccarello^{54,44}

¹Centro Atómico Bariloche and Instituto Balseiro (CNEA-UNCuyo-CONICET), San Carlos de Bariloche, Argentina

²Centro de Investigaciones en Láseres y Aplicaciones, CITEDEF and CONICET, Villa Martelli, Argentina

³Departamento de Física and Departamento de Ciencias de la Atmósfera y los Océanos, FCEyN, Universidad de Buenos Aires and CONICET, Buenos Aires, Argentina

⁴IFLP, Universidad Nacional de La Plata and CONICET, La Plata, Argentina

- ⁵Instituto de Astronomía y Física del Espacio (IAFE, CONICET-UBA), Buenos Aires, Argentina
- ⁶Instituto de Física de Rosario (IFIR) – CONICET/U.N.R. and Facultad de Ciencias Bioquímicas y Farmacéuticas U.N.R., Rosario, Argentina
- ⁷Instituto de Tecnologías en Detección y Astropartículas (CNEA, CONICET, UNSAM), and Universidad Tecnológica Nacional – Facultad Regional Mendoza (CONICET/CNEA), Mendoza, Argentina
- ⁸Instituto de Tecnologías en Detección y Astropartículas (CNEA, CONICET, UNSAM), Buenos Aires, Argentina
- ⁹Observatorio Pierre Auger, Malargüe, Argentina
- ¹⁰Observatorio Pierre Auger and Comisión Nacional de Energía Atómica, Malargüe, Argentina
- ¹¹Universidad Tecnológica Nacional – Facultad Regional Buenos Aires, Buenos Aires, Argentina
- ¹²University of Adelaide, Adelaide, S.A., Australia
- ¹³Université Libre de Bruxelles (ULB), Brussels, Belgium
- ¹⁴Vrije Universiteit Brussels, Brussels, Belgium
- ¹⁵Centro Brasileiro de Pesquisas Físicas, Rio de Janeiro, RJ, Brazil
- ¹⁶Centro Federal de Educação Tecnológica Celso Suckow da Fonseca, Nova Friburgo, Brazil
- ¹⁷Universidade de São Paulo, Escola de Engenharia de Lorena, Lorena, SP, Brazil
- ¹⁸Universidade de São Paulo, Instituto de Física de São Carlos, São Carlos, SP, Brazil
- ¹⁹Universidade de São Paulo, Instituto de Física, São Paulo, SP, Brazil
- ²⁰Universidade Estadual de Campinas, IFGW, Campinas, SP, Brazil
- ²¹Universidade Estadual de Feira de Santana, Feira de Santana, Brazil
- ²²Universidade Federal do ABC, Santo André, SP, Brazil
- ²³Universidade Federal do Paraná, Setor Palotina, Palotina, Brazil
- ²⁴Universidade Federal do Rio de Janeiro, Instituto de Física, Rio de Janeiro, RJ, Brazil
- ²⁵Universidade Federal do Rio de Janeiro (UFRJ), Observatório do Valongo, Rio de Janeiro, RJ, Brazil
- ²⁶Universidade Federal Fluminense, EEIMVR, Volta Redonda, RJ, Brazil
- ²⁷Universidad de Medellín, Medellín, Colombia
- ²⁸Universidad Industrial de Santander, Bucaramanga, Colombia
- ²⁹Charles University, Faculty of Mathematics and Physics, Institute of Particle and Nuclear Physics, Prague, Czech Republic
- ³⁰Institute of Physics of the Czech Academy of Sciences, Prague, Czech Republic
- ³¹Palacky University, RCPTM, Olomouc, Czech Republic
- ³²Institut de Physique Nucléaire d'Orsay (IPNO), Université Paris-Sud, Univ. Paris/Saclay, CNRS-IN2P3, Orsay, France
- ³³Laboratoire de Physique Nucléaire et de Hautes Energies (LPNHE), Universités Paris 6 et Paris 7, CNRS-IN2P3, Paris, France
- ³⁴Univ. Grenoble Alpes, CNRS, Grenoble Institute of Engineering Univ. Grenoble Alpes, LPSC-IN2P3, 38000 Grenoble, France, France
- ³⁵Bergische Universität Wuppertal, Department of Physics, Wuppertal, Germany
- ³⁶Karlsruhe Institute of Technology, Institute for Experimental Particle Physics (ETP), Karlsruhe, Germany

- ³⁷Karlsruhe Institute of Technology, Institut für Kernphysik, Karlsruhe, Germany
- ³⁸Karlsruhe Institute of Technology, Institut für Prozessdatenverarbeitung und Elektronik, Karlsruhe, Germany
- ³⁹RWTH Aachen University, III. Physikalisches Institut A, Aachen, Germany
- ⁴⁰Universität Hamburg, II. Institut für Theoretische Physik, Hamburg, Germany
- ⁴¹Universität Siegen, Fachbereich 7 Physik – Experimentelle Teilchenphysik, Siegen, Germany
- ⁴²Gran Sasso Science Institute, L’Aquila, Italy
- ⁴³INFN Laboratori Nazionali del Gran Sasso, Assergi (L’Aquila), Italy
- ⁴⁴INFN, Sezione di Catania, Catania, Italy
- ⁴⁵INFN, Sezione di Lecce, Lecce, Italy
- ⁴⁶INFN, Sezione di Milano, Milano, Italy
- ⁴⁷INFN, Sezione di Napoli, Napoli, Italy
- ⁴⁸INFN, Sezione di Roma “Tor Vergata”, Roma, Italy
- ⁴⁹INFN, Sezione di Torino, Torino, Italy
- ⁵⁰Osservatorio Astrofisico di Torino (INAF), Torino, Italy
- ⁵¹Politecnico di Milano, Dipartimento di Scienze e Tecnologie Aerospaziali, Milano, Italy
- ⁵²Università del Salento, Dipartimento di Matematica e Fisica “E. De Giorgi”, Lecce, Italy
- ⁵³Università dell’Aquila, Dipartimento di Scienze Fisiche e Chimiche, L’Aquila, Italy
- ⁵⁴Università di Catania, Dipartimento di Fisica e Astronomia, Catania, Italy
- ⁵⁵Università di Milano, Dipartimento di Fisica, Milano, Italy
- ⁵⁶Università di Napoli “Federico II”, Dipartimento di Fisica “Ettore Pancini”, Napoli, Italy
- ⁵⁷Università di Roma “Tor Vergata”, Dipartimento di Fisica, Roma, Italy
- ⁵⁸Università Torino, Dipartimento di Fisica, Torino, Italy
- ⁵⁹Benemérita Universidad Autónoma de Puebla, Puebla, México
- ⁶⁰Centro de Investigación y de Estudios Avanzados del IPN (CINVESTAV), México, D.F., México
- ⁶¹Unidad Profesional Interdisciplinaria en Ingeniería y Tecnologías Avanzadas del Instituto Politécnico Nacional (UPIITA-IPN), México, D.F., México
- ⁶²Universidad Autónoma de Chiapas, Tuxtla Gutiérrez, Chiapas, México
- ⁶³Universidad Nacional Autónoma de México, México, D.F., México
- ⁶⁴Institute of Nuclear Physics PAN, Krakow, Poland
- ⁶⁵University of Łódź, Faculty of Astrophysics, Łódź, Poland
- ⁶⁶University of Łódź, Faculty of High-Energy Astrophysics, Łódź, Poland
- ⁶⁷Laboratório de Instrumentação e Física Experimental de Partículas – LIP and Instituto Superior Técnico – IST, Universidade de Lisboa – UL, Lisboa, Portugal
- ⁶⁸“Horia Hulubei” National Institute for Physics and Nuclear Engineering, Bucharest-Magurele, Romania
- ⁶⁹Institute of Space Science, Bucharest-Magurele, Romania
- ⁷⁰University Politehnica of Bucharest, Bucharest, Romania
- ⁷¹Center for Astrophysics and Cosmology (CAC), University of Nova Gorica, Nova Gorica, Slovenia
- ⁷²Experimental Particle Physics Department, J. Stefan Institute, Ljubljana, Slovenia
- ⁷³Universidad de Granada and C.A.F.P.E., Granada, Spain

- ⁷⁴Instituto Galego de Física de Altas Enerxías (I.G.F.A.E.), Universidad de Santiago de Compostela, Santiago de Compostela, Spain
- ⁷⁵IMAPP, Radboud University Nijmegen, Nijmegen, The Netherlands
- ⁷⁶KVI – Center for Advanced Radiation Technology, University of Groningen, Groningen, The Netherlands
- ⁷⁷Nationaal Instituut voor Kernfysica en Hoge Energie Fysica (NIKHEF), Science Park, Amsterdam, The Netherlands
- ⁷⁸Stichting Astronomisch Onderzoek in Nederland (ASTRON), Dwingeloo, The Netherlands
- ⁷⁹Universiteit van Amsterdam, Faculty of Science, Amsterdam, The Netherlands
- ⁸⁰Case Western Reserve University, Cleveland, OH, USA
- ⁸¹Colorado School of Mines, Golden, CO, USA
- ⁸²Department of Physics and Astronomy, Lehman College, City University of New York, Bronx, NY, USA
- ⁸³Louisiana State University, Baton Rouge, LA, USA
- ⁸⁴Michigan Technological University, Houghton, MI, USA
- ⁸⁵New York University, New York, NY, USA
- ⁸⁶Pennsylvania State University, University Park, PA, USA
- ⁸⁷University of Chicago, Enrico Fermi Institute, Chicago, IL, USA
- ⁸⁸University of Delaware, Department of Physics and Astronomy, Newark, USA
- ⁸⁹University of Nebraska, Lincoln, NE, USA

^aSchool of Physics and Astronomy, University of Leeds, Leeds, United Kingdom

^bMax-Planck-Institut für Radioastronomie, Bonn, Germany

^cFermi National Accelerator Laboratory, USA

^dalso at Universidade Federal de Alfenas, Poços de Caldas, Brazil

^eColorado State University, Fort Collins, CO, USA

^fnow at Institute for Cosmic Ray Research, University of Tokyo

^galso at Karlsruhe Institute of Technology, Karlsruhe, Germany

^halso at University of Bucharest, Physics Department, Bucharest, Romania

E-mail: auger_spokespersons@fnal.gov

Abstract. The profile of the longitudinal development of showers produced by ultra-high energy cosmic rays carries information related to the interaction properties of the primary particles with atmospheric nuclei. In this work, we present the first measurement of the average shower profile in traversed atmospheric depth at the Pierre Auger Observatory. The shapes of profiles are well reproduced by the Gaisser-Hillas parametrization within the range studied, for $E > 10^{17.8}$ eV. A detailed analysis of the systematic uncertainties is performed using 10 years of data and a full detector simulation. The average shape is quantified using two variables related to the width and asymmetry of the profile, and the results are compared with predictions of hadronic interaction models for different primary particles.

Contents

1	Introduction	1
2	Event reconstruction at the Pierre Auger Observatory	2
3	Average longitudinal shower profile	3
4	Data selection and Monte Carlo validation	5
5	Systematic uncertainties	8
6	Results	9
7	Summary	11

1 Introduction

Ultra-High Energy Cosmic Rays (UHECRs) are the most energetic particles known in the Universe. The study of the cascades resulting from their interactions with atmospheric nuclei can provide a unique glimpse into hadronic interaction properties at center-of-mass energies more than one order of magnitude above those attained in human-made colliders. The collision of a UHECR with an atmospheric nucleus initiates an extensive air shower of secondary particles developing in the traversed air mass, usually referred to as slant depth, X .

In a high-energy hadronic interaction, most of the secondary particles are pions, of which around one third are π^0 mesons. These immediately decay into two photons and initiate an electromagnetic cascade that is dominated by e^\pm and γ . The charged pions, along with the other secondary hadrons produced in smaller numbers such as kaons and protons/neutrons, constitute the hadronic cascade. Since the interactions of e^\pm and γ yield virtually no hadrons, an air shower can be considered as the sum of two independent cascades: a hadronic cascade, waning as it penetrates further in the atmosphere losing energy via the decay of neutral pions, and an electromagnetic cascade that is constantly being fed by the hadronic counterpart. After only a few generations the vast majority of the total energy of the primary particle has been transferred to the electromagnetic part of the cascade.

The cascade progresses until the average energy of single e^\pm and γ particles falls below the critical energy at which energy is lost predominantly by collisions instead of radiative processes. Atmospheric nitrogen molecules are excited by the passage of charged particles, and the subsequent nitrogen de-excitation results in the emission of a quantity of fluorescence light which is proportional to the energy lost by the shower electrons. The energy deposited by an air shower as a function of the traversed depth is known as its longitudinal profile, which can be measured by the detection of fluorescent light at the ground.

The integral of the longitudinal profile gives a calorimetric measurement of the shower energy. To measure this energy, we need to estimate the full profile. A functional form must be used to extrapolate outside the observed region. The atmospheric depth at which the profile has a maximum, X_{\max} , is the variable most sensitive to the cross-section of the first interaction and to the mass of the primary particle. The precise shape of the energy deposit

profile, however, has remained largely untested. This paper describes the first measurement of the shape of the longitudinal profile as a function of traversed atmospheric depth for UHECRs with energies above $10^{17.8}$ eV. While measured profiles for individual events often have large uncertainties, particularly at values far from the maximum, in this work a high precision is achieved by averaging, in energy bins, showers detected by the fluorescence detectors of the Pierre Auger Observatory.

The motivation for this measurement is three-fold. The first is to cross-check the assumption that shower profiles are well described by the currently used parametrization. The second is to provide a new way to control the quality of the shower reconstruction for the fluorescence detector. The third is to use the shape parameters to make new independent tests on hadronic interaction models and analysis of primary cosmic-ray composition.

This paper is organized as follows. The Pierre Auger Observatory and the event reconstruction procedure are described in section 2. In section 3, the functional form used to fit the average profiles is defined, with its two variables and their interpretation. In section 4, we show how the average longitudinal profiles are reconstructed. The analysis is validated by comparing the average profiles obtained after full detector simulation and data reconstruction to the ones calculated directly from the simulated energy deposits in the atmosphere. The systematic uncertainties associated with the measurement are estimated in section 5. Finally, the results of the fit are presented in section 6, and the shape variables measured at each energy are compared to the expectations for proton and iron initiated showers obtained from different hadronic interaction models.

2 Event reconstruction at the Pierre Auger Observatory

The Pierre Auger Observatory [1] is a hybrid detector, consisting of a 3000 km^2 Surface Detector (SD) overlooked by the Fluorescence Detector (FD). The SD is composed of 1600 water-Cherenkov detectors separated by 1.5 km. The FD consists of four sites with six telescopes each. The field of view of each telescope spans 30° in azimuth and ranges from 1.5° to 30° in elevation. Three additional telescopes called HEAT (High Elevation Auger Telescope) cover the elevation range from 30° to 60° . This range is important for showers with energies lower than the ones studied in this paper and thus HEAT data were not used here.

The measurement of atmospheric properties is essential for the reconstruction of the air showers measured by the detectors mentioned above. The molecular properties (temperature, humidity and pressure height profiles) are provided by the Global Data Assimilation System in three-hour intervals [2]. The aerosol content is monitored hourly by calibrated laser shots from two laser facilities located near the center of the SD array, and cross-checked by LIDAR stations at each FD site. Cloud coverage in the shower path is measured by the LIDAR and cloud cameras at each site (every 15 and every 5 minutes, respectively), and complemented with data from the Geostationary Operational Environmental Satellite (GOES).

The reconstruction of shower profiles from FD data proceeds in the following steps (see e.g. [1]). Firstly, the shower-detector plane, spanned by the pointing directions of pixels in the shower image, is calculated. The shower axis within this plane is obtained using the timing information of each pixel, as well as the timing of the closest SD station with signal (hybrid reconstruction).

For each time bin, a vector pointing from the telescope to the shower is defined, and the signals of all photomultipliers (PMTs) pointing to the same direction within a given opening

angle are summed. This angle is determined event-by-event by maximizing the ratio of the signal to the accumulated noise from the night sky background.

Given the reconstructed geometry, the signal at each time bin can be converted into an energy deposited by the shower at a given slant depth. Every time bin i is projected to a path of length l_i along the shower track. The slant depth, X_i , is inferred by integrating the atmospheric density through l_i . During its path from the shower axis to the FD, light is attenuated due to Rayleigh scattering on air and Mie scattering on aerosols. The light emitted on the shower track at time bin i can be calculated from the measured light at the aperture corrected by this attenuation factor.

The detected photons correspond to different light emission mechanisms and can reach the telescope directly or by scattering in the atmosphere. Fluorescence light is emitted isotropically along the shower track. High-energy charged particles emit Cherenkov light in a forward-concentrated beam. Even if the shower does not point directly to the detector, a fraction of this beam will be scattered into the field of view. This fraction is calculated taking into account the characteristics of both molecular and aerosol scattering in the atmosphere.

The Cherenkov and fluorescence light produced by an air shower are connected to the energy deposit by a set of linear equations [3]. The profile of energy deposit as a function of slant depth is functionally described by the Gaisser-Hillas parametrization [4],

$$f_{\text{GH}}(X) = (dE/dX)_{\text{max}} \left(\frac{X - X_0}{X_{\text{max}} - X_0} \right)^{\frac{X_{\text{max}} - X_0}{\lambda}} \exp \left(-\frac{X_{\text{max}} - X}{\lambda} \right), \quad (2.1)$$

which has four parameters: the maximum energy deposit, $(dE/dX)_{\text{max}}$, the depth at which this maximum is reached, X_{max} , and shape parameters X_0 and λ . This function is used in the calculation of the Cherenkov beam accumulated up to X_i , which determines the number of Cherenkov photons seen at the aperture. The proportionality between the number of fluorescence photons and the energy deposit is given by the fluorescence yield [5], which depends on the molecular properties of the atmosphere. The statistical uncertainty in dE/dX_i is calculated from the Poisson uncertainty of photoelectrons detected by the photomultipliers of the fluorescence telescopes.

The four parameters that describe the shower profile and their uncertainties are obtained from a log-likelihood fit to the number of photoelectrons detected at the PMTs. The calorimetric energy is the integral of f_{GH} , and the total energy of the shower is estimated by correcting for the *invisible* energy carried away by neutrinos and high-energy muons.

3 Average longitudinal shower profile

The maximum energy deposit of the longitudinal profile, $(dE/dX)_{\text{max}}$, is proportional to the energy of the primary particle and varies by three orders of magnitude in the energy range studied in this work. The X_{max} value of each shower is, on average, a characteristic of the primary particle mass, but it varies greatly also for showers with the same primary, due to the depth at which the first interaction occurs, the large phase space for high-energy interactions and the general stochastic nature of shower development.

The focus of this work is to separate these two parameters, $(dE/dX)_{\text{max}}$ and X_{max} , to isolate the information contained in the profile shape itself. First, each measured shower profile is normalized to its fitted $(dE/dX)_{\text{max}}$. With this rescaling, all showers have a maximum value at 1. Then, the showers are transformed to the same development stage by translating

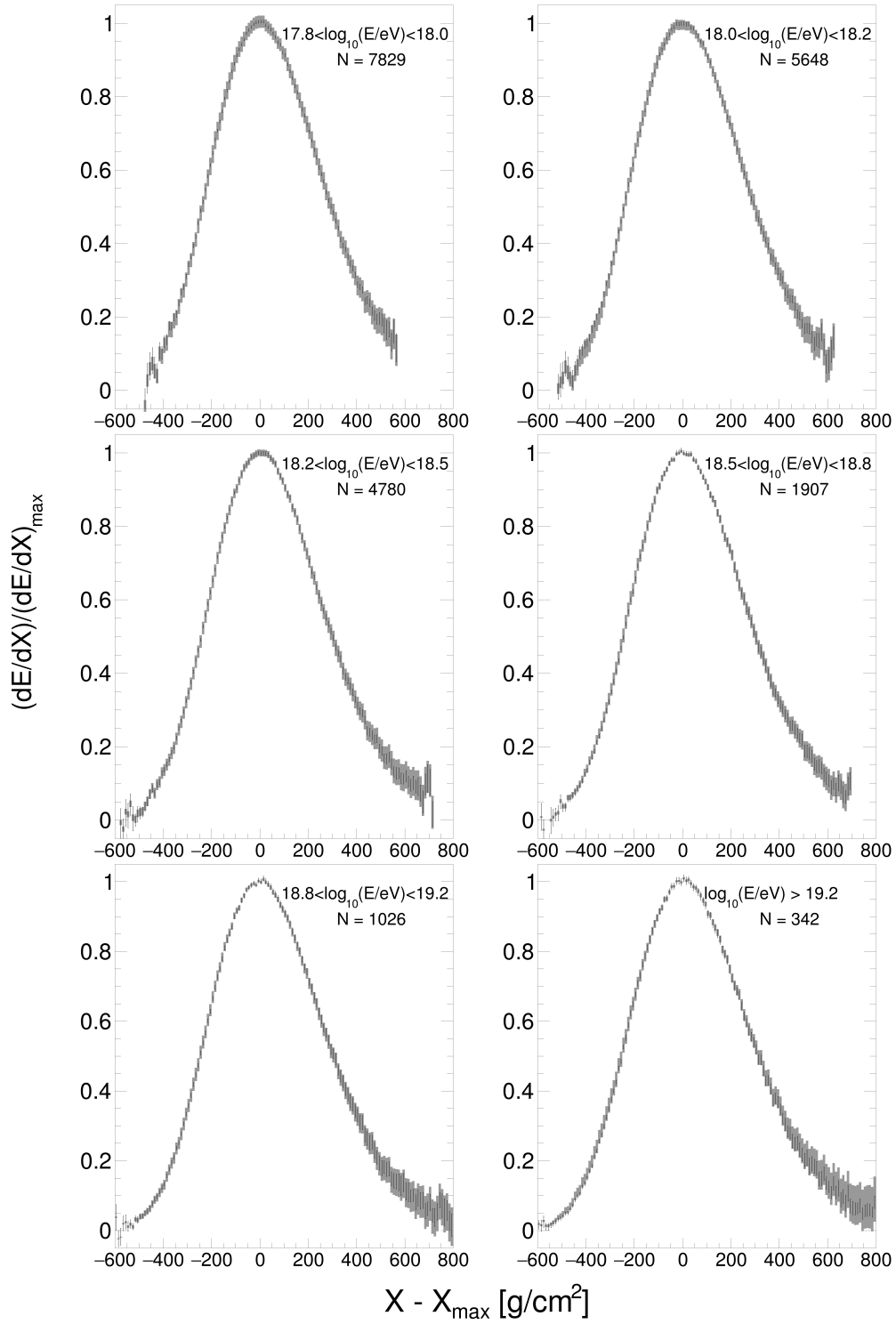


Figure 1. Average longitudinal shower profiles for the selected data set, divided into the six energy bins used in this work (see legend for limits and number of events). The data is shown with statistical errors as a black line and an estimated bin-by-bin systematic uncertainty as a gray area.

the slant depth by X_{\max} , i.e., $X' \equiv X - X_{\max}$, thus all profiles are centered at zero. The normalized energy deposit profile, with $(dE/dX)' \equiv (dE/dX)/(dE/dX)_{\max}$, can be described by the Gaisser-Hillas function, written as a function of parameters R and L [6],

$$(dE/dX)' = \left(1 + R \frac{X'}{L}\right)^{R-2} \exp\left(-\frac{X'}{RL}\right), \quad (3.1)$$

where $R = \sqrt{\lambda/|X'_0|}$, $L = \sqrt{|X'_0|\lambda}$ and $X'_0 \equiv X_0 - X_{\max}$. In this notation, the Gaisser-Hillas function is a Gaussian with standard deviation L , multiplied by a term that distorts it, with the asymmetry governed by R , and thus these parameters are less correlated than λ and X_0 . An equivalent parametrization as a function of the Full Width at Half Maximum, f_{FWHM} , and asymmetry, f , has been reached independently [7].

Note that in previous analyses by the HiRes/MIA [8] and HiRes Collaborations [9], the energy deposit profile was constructed as a function of shower age ($s = 3X/(X + 2X_{\max})$), and the resulting shapes were found to be compatible with a Gaussian distribution with standard deviation σ_{age} . This width, however, is convolved with (and dominated by) the X_{\max} value¹. In this work we chose to represent the profiles in atmospheric depth because it preserves the measured event-by-event shape. Also, R and L taken from the fit to the profiles in atmospheric depth have been shown to be sensitive to the mass of the primary cosmic rays and to the properties of the high-energy interactions that occur at the start of the shower. The sensitivity is kept by an average profile [10], i.e., the average shape of a sample of profiles initiated by different primary particles is related to the average mass composition in the sample.

4 Data selection and Monte Carlo validation

The event selection used here is based on the selection criteria developed by the Pierre Auger Collaboration to measure the X_{\max} distributions [11], and is applied to data covering the period from January 2004 to March 2015. Good weather conditions are required, with no clouds in the sky and a measured vertical aerosol optical depth lower than 0.1 at a height of 3 km. A good hybrid geometry reconstruction is essential for the profile reconstruction: only events with at least one triggered water-Cherenkov detector closer than 1500 m from the core, and for which the probability of detecting both proton and iron primaries is above 95%, are accepted. On the measured longitudinal profile, strict cuts are made: at least 300 g/cm² must be observed, including the X_{\max} depth, for which the expected resolution must be less than 40 g/cm². A fiducial field of view is defined to guarantee a uniform acceptance over a range in X_{\max} that covers the majority of the X_{\max} distribution. Moreover, to minimize the amount of Cherenkov light, the minimum angle between the shower axis and the pointing vector of any of the pixels with signal has to be larger than 20°.

In this work, two additional selection cuts with respect to the criteria developed in [11] were applied. When showers cross two telescopes, differences in alignment cause time residuals in the geometry fit, as the distance to the shower estimated by both telescopes is different. The estimation of the atmospheric attenuation depends on the distance and, therefore, also the

¹ Shower age is defined as $s(X') = 1 + \frac{2X'}{3X_{\max} - X'}$. As L is the profile width in depth, a relation between σ_{age} and L can be found by making $X' = \pm L$ in the previous formula. Doing the derivative with respect to L and X_{\max} , we find that $\left(\frac{\partial \sigma_{\text{age}}}{\partial L} \Delta(L)\right) / \left(\frac{\partial \sigma_{\text{age}}}{\partial X_{\max}} \Delta(X_{\max})\right) = \frac{X_{\max} \Delta(L)}{L \Delta(X_{\max})} \approx 1/6$, where Δ stands for the proton-iron difference in each variable. So the majority of the composition separation in σ_{age} comes from X_{\max} .

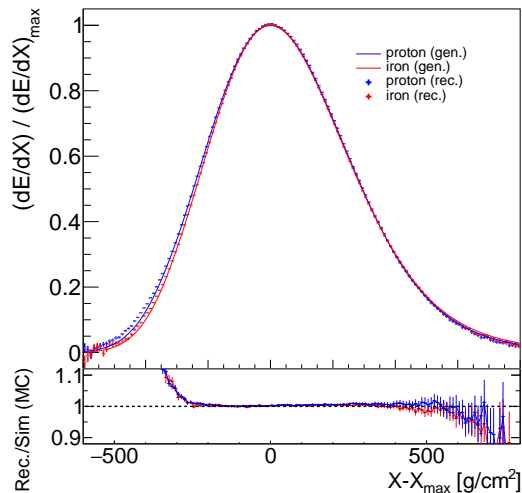


Figure 2. Average longitudinal shower profile for simulated events with energies between $10^{18.8}$ and $10^{19.2}$ eV. The profiles for proton and iron are shown in blue and red, respectively. In the bottom plot, the ratio of reconstructed profiles to the generated ones is shown.

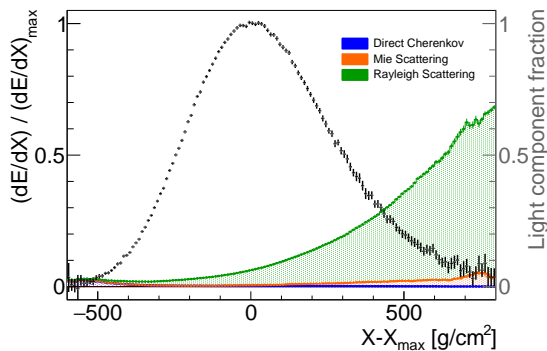


Figure 3. Average longitudinal shower profile for data events with energies between $10^{18.8}$ and $10^{19.2}$ eV. The measured normalized energy deposit is shown in black. The colored regions (detailed in the legend) represent the average fraction of direct and scattered Cherenkov light in the photons measured at the telescope aperture, computed in the individual shower reconstruction.

energy deposit is affected. Large residuals were found in one of the telescopes (Coihueco 6), so events in which the profiles were measured using this telescope are excluded. Also, events for which the pixel time-fit used to determine the shower axis yielded very large reduced χ^2 values (above 5) are excluded. The first cut affects approximately 3% of the events (649), while in the second only two events are excluded.

In total, 21532 events are selected for analysis. These are divided into six energy bins. The shower profiles are constructed in 10 g/cm^2 bins in X' , in which each energy deposit is accumulated with a weight corresponding to the inverse of its squared error. The average profiles for all energies are shown in figure 1.

The reconstruction and analysis of the average longitudinal shower profiles was validated with a full detector simulation for energies between $10^{17.8}$ and 10^{20} eV with proton and iron

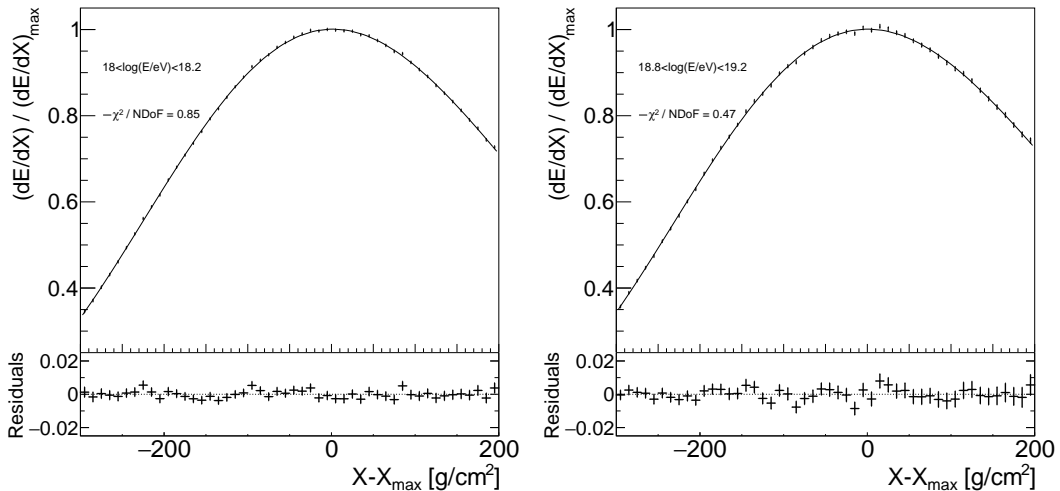


Figure 4. Measured average longitudinal shower profiles for energies between 10^{18} and $10^{18.2}$ eV (left) and between $10^{18.8}$ and $10^{19.2}$ eV (right). Data is shown in black, together with the Gaisser-Hillas fit to the profile. The residuals of the fit are shown in the bottom insets.

as primary particles. Comparing simulated and reconstructed showers an excellent agreement is found for the central part, but reconstruction increasingly deviates for negative X' , and a lower bound should be set for the analysis. At depths beyond X_{\max} , showers lose most of the primary information, but the later parts of the profile are necessary to measure the profile width. An upper bound should maximize the relative importance of the profile start while keeping the statistical uncertainty on L and R below the proton/iron separation. While no detailed optimization was attempted for this first measurement, common bounds for all energies were set at $[-300, +200]$ g/cm^2 , fulfilling the above requirements.

Figure 2 shows the generated and reconstructed profiles for proton and iron simulations for energies around 10^{19} eV; figure 3 shows the data reconstruction for the same energy bin, together with the different light components along the profile. Note that the chosen fit region is dominated by fluorescence light, directly proportional to the shower energy deposit along X .

The shower profiles are fitted with equation 3.1, leaving all parameters unconstrained. In addition to R and L , the normalization and the maximum position are allowed to vary around $(dE/dX)' = 1$ and $X' = 0$ g/cm^2 to account for possible effects of smearing due to X_{\max} resolution and bias in the energy deposit. The results for data are within the predictions from full-detector simulation of showers, i.e., at all energies the normalization is unitary within 0.5% and the maximum position is within ± 1 g/cm^2 .

The values of the shape parameters obtained by fitting the average profile at generator level and after full detector simulation and shower reconstruction are compatible for all energies above 10^{18} eV, with a larger difference for the first energy bin ($10^{17.8}$ to 10^{18} eV) – but even at this energy the fitted values are always within 0.005 for R and 2 g/cm^2 for L . The values of R and L for data are corrected by the average bias obtained from proton and iron simulations, and half of the correction is added as systematic uncertainty.

	R	L [g/cm ²]
Atmosphere	0.030	5.5
Light components & fit	0.018	3.3
Geometry	0.018	2.2
Detector	0.012	1.8
Bias correction & Energy scale	0.010	1.0
Total	0.040	7.3
Statistical	0.012	0.9

Table 1. Breakdown of systematic uncertainties for R and L . Uncertainties are energy dependent and asymmetric, so only the largest value is reported.

5 Systematic uncertainties

The reconstruction of longitudinal profiles from the measurements at the FD requires several steps with which systematic uncertainties are associated. This section describes the effects we have considered, which are summarized in table 1.

Atmospheric conditions play a crucial role in the propagation of the light from the shower to the fluorescence detector [12]. Several systematic uncertainties related to this process were studied. They included the impact of possible patches of clouds in the sky, differences found when separating data by the seasons of the year, and uncertainties in the overall aerosol content and its height dependence. The atmospheric aerosol attenuation, $\tau_A(h)$, is measured hourly with the central laser facility [13, 14]. The measurement compares the number of photons detected on the FD (as a function of height) in a given laser run with the one detected on a clear reference night. The aerosol height profile on the shower path can be calculated from $\tau_A(h)$, but has two main sources of uncertainty: the determination of the aerosol profile on the reference night (which is fixed for all showers) and the propagation of the uncertainty on the laser measurement at the FD to the path to each air shower (which varies from bin to bin and depends on geometry and atmospheric conditions). The uncertainty related to the estimation of the aerosol content was found to be the largest in this work, yielding approximately a ± 0.02 and ± 5 g/cm² uncertainty in R and L , respectively.

The uncertainties in the determination of the different light components were also considered. First, the reconstruction was repeated changing the fluorescence and Cherenkov yield values within their uncertainties (4% and 5%, respectively), and accounting or not for the multiple scattering corrections. Then, the data was separated according to the fluorescence fraction of the event, which gave a larger systematic difference. When only showers with fluorescence fractions lower than 90% (the average value for the analyzed sample) are used, the resulting average profile is 2 g/cm² larger in width, L , while the change in R is negligible.

The fit of the longitudinal profile of individual events is constrained in the integral of the normalized longitudinal profile, by an energy dependent value taken from shower simulations. Furthermore, the Gaisser-Hillas parameters are constrained by $X_0 = -121 \pm 172$ g/cm² and $\lambda = 61 \pm 13$ g/cm², values found previously in a small ensemble of very high-energy events with long tracks in the FD for which the unconstrained fit was possible [11]. The uncertainty in the estimation of the profile constraints was propagated in the reconstruction by shifting the central values by their standard deviation. This contribution is relatively more important in L (around 3 g/cm²) than in R (0.01).

The reconstructed shower geometry is given first by the zenith and azimuth angles

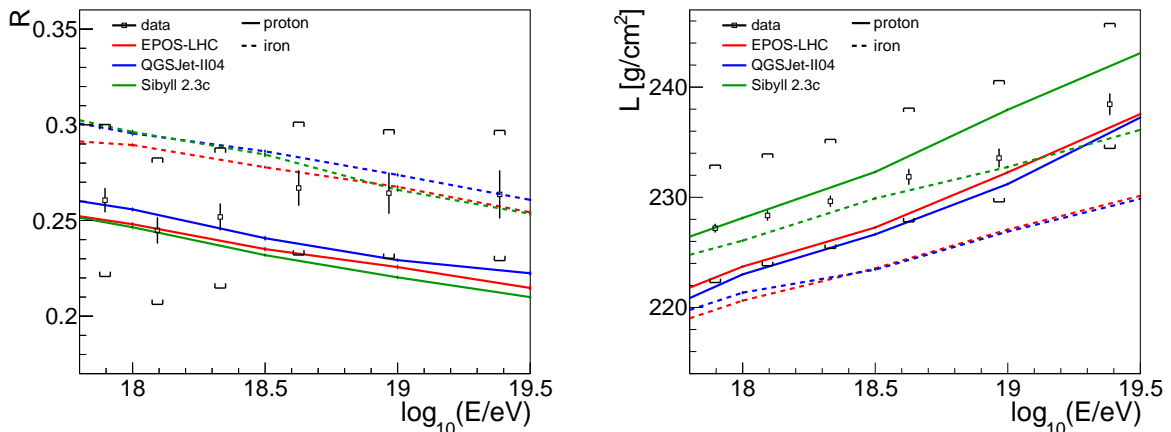


Figure 5. R (left) and L (right) as a function of energy. The data are shown in black, with the vertical line representing the statistical error and the brackets the systematic uncertainty. Hadronic interaction models simulated with CORSIKA are shown (see legend), with full lines being proton and dashed lines iron predictions.

of the shower-detector plane, and then the shower axis is defined by distance, angle and time references. All these five parameters are varied within $\pm 1\sigma$ to obtain the systematic uncertainty associated with the reconstructed shower geometry. To ensure the quality of the reconstruction, the dependence of R and L on the zenith angle or distance from X_{\max} to the telescope was also studied, but was found to be small and contained in the geometric systematic uncertainty of around 2 g/cm^2 in L and 0.02 in R .

The effect of the uncertainty in telescope alignment was also considered. One of the telescopes had been previously excluded from the analysis by looking directly at residuals in the timing at the crossing between telescopes. Smaller effects were tested by studying the telescope-to-telescope difference of the reconstructed shape. These are smaller than other systematic uncertainties, but at the level of 0.012 in R and 1.8 g/cm^2 in L .

Finally, the uncertainty of the energy scale of 14% [15] and the previously described proton-iron discrepancy from the bias correction are also added, but they are small (below 1 g/cm^2 in L and 0.01 in R) in comparison with the previously described ones.

The uncertainties vary with energy and are asymmetric. Table 1 shows the largest value for each category, and table 2 shows the total error per energy bin.

6 Results

The fit of data profiles with the Gaisser-Hillas parametrization is shown in figure 4. The fitted function follows the data points through the depth range used in this work, $[-300, +200] \text{ g/cm}^2$, with residuals within the statistical uncertainties. This is the first experimental demonstration that the Gaisser-Hillas parametrization is an accurate functional form to describe the central part of UHECR longitudinal profiles above $10^{17.8} \text{ eV}$ at 1% accuracy.

The values of R and L obtained from the fit for the six energy intervals studied are shown in table 2, along with their energy dependent statistical and systematic uncertainties. The average energy and number of events, N , in each bin are also listed for reference.

The existing hadronic interaction models give different predictions for the shape variables. CORSIKA [16] was used to simulate proton, helium, nitrogen and iron showers with

Energy [eV]	$\langle \log_{10}[E/\text{eV}] \rangle$	N	R			L [g/cm ²]		
			$\langle value \rangle$	stat.	syst.	$\langle value \rangle$	stat.	syst.
$10^{17.8} - 10^{18.0}$	17.90	7829	0.260	0.006	$^{+0.039}_{-0.040}$	226.2	0.4	$^{+5.7}_{-4.9}$
$10^{18.0} - 10^{18.2}$	18.09	5648	0.244	0.007	$^{+0.037}_{-0.039}$	227.6	0.4	$^{+5.6}_{-4.5}$
$10^{18.2} - 10^{18.5}$	18.33	4780	0.252	0.007	$^{+0.035}_{-0.037}$	229.1	0.5	$^{+5.6}_{-4.3}$
$10^{18.5} - 10^{18.8}$	18.63	1907	0.267	0.009	$^{+0.034}_{-0.035}$	231.4	0.7	$^{+6.2}_{-4.1}$
$10^{18.8} - 10^{19.2}$	18.97	1026	0.264	0.010	$^{+0.033}_{-0.034}$	233.3	0.8	$^{+7.0}_{-4.0}$
$> 10^{19.2}$	19.38	342	0.264	0.012	$^{+0.023}_{-0.035}$	238.3	0.9	$^{+7.3}_{-4.0}$

Table 2. R and L values for each of the measured energy bins, along with the statistical and systematic uncertainties.

the EPOS-LHC [17], QGSJetII-04 [18] and Sibyll2.3c [19] models. The evolution of R and L with energy, along with their respective systematic and statistical uncertainties, is shown in figure 5. Both the asymmetry, R , and the width, L , in data agree well with the predicted values for all models. For the asymmetry, all models give similar predictions, and the results seem to point to the composition becoming heavier with energy, although current systematic uncertainties still hinder any composition claim. For L , data is consistent with a linear increase with $\log_{10}(E/\text{eV})$. L is compatible with the predictions of Sibyll2.3c for all compositions, but points to a lighter composition if compared with the other two models, that predict smaller values of L .

To understand better the interplay of the two measured variables, it is interesting to see the results in the (R, L) plane for two fixed energies (figure 6). In these plots, all composition scenarios are represented (as a combination of proton, He, N and Fe) for a given energy. For all models, proton has a lower R and larger L than iron, so moving from the top left to the bottom right points within a given model, makes the transition from lighter to heavier primaries. It is interesting, however, to note that the areas have different shapes: some models predict, at a given energy, a smaller L for proton than for Helium, while others do the opposite.

Since R and L are experimentally correlated, these plots provide a smaller phase space within which to constrain the predictions of the hadronic interaction models. In figure 6, for the 10^{18} eV energy bin (left), it can be seen that the average value in data is in the area occupied by most models for a light composition, while at 10^{19} eV (right) it is within the predictions for intermediate mass primaries.

Within the current experimental resolution, the data are fully compatible with most composition scenarios at the 2σ level for all models. It is, however, interesting to note that Sibyll2.3c occupies a different phase space than the other two post-LHC models, indicating that a higher precision measurement of the profile shape could provide a test on the hadronic interaction models.

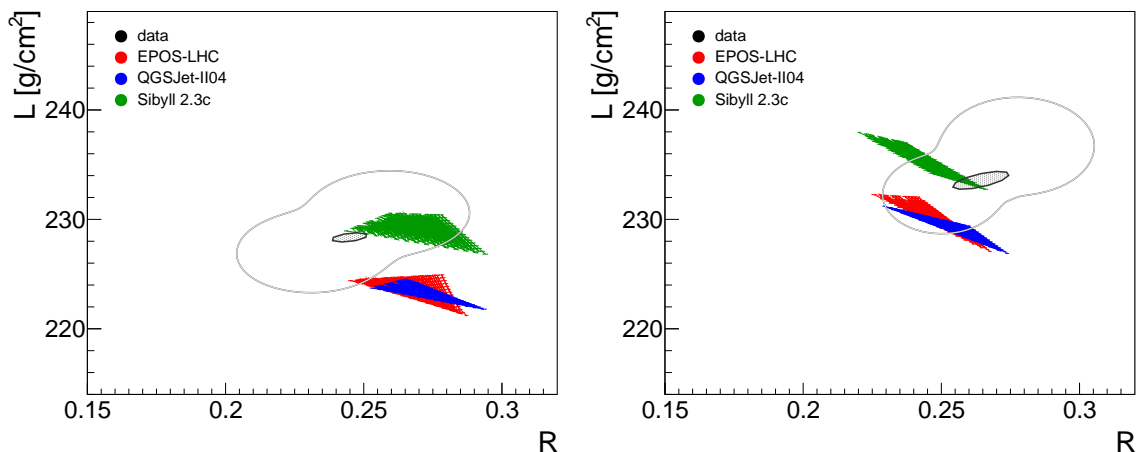


Figure 6. L vs R for the energy bin 10^{18} to $10^{18.2}$ eV (left) and from $10^{18.8}$ to $10^{19.2}$ eV (right). The inner dark grey ellipse shows the fitted value for data and its statistical uncertainty, and the outer light grey line the systematic uncertainty. For each hadronic model proton, helium, nitrogen and iron showers were simulated and average profiles were built making all possible combinations. Each of the points represents the value of R and L for a given model and composition combination, so the phase space spanned by each model is contained in its respective colored area. Pure proton is, for each model, on the upper left side (low R and high L) and the transition to iron goes gradually to the lower right side.

7 Summary

In this work, the Pierre Auger Observatory has been used to measure the average shape of the longitudinal profile of air showers. The method was first validated in a full detector simulation of proton and iron primaries, which showed that reconstructed and simulated profiles are in very good agreement for all energies above $10^{17.8}$ eV. The average longitudinal profiles as a function of atmospheric depth of ultra-high energy cosmic rays have been presented for the first time. They are well described by a Gaisser-Hillas function throughout the fitting range chosen, -300 to $+200$ g/cm² around the shower maximum, to a 1% level precision.

The systematic uncertainties contributing to the measurement were estimated, and we found that the uncertainty in the atmospheric aerosol content is the main factor affecting the shape of the reconstructed longitudinal profile. In fact, the variations of L and R values obtained when dividing the sample according to different detection conditions are all within the range allowed by the atmospheric uncertainty. The validation of the profile shape around the shower maximum increases our confidence in its use for the determination of the shower calorimetric energy and of the X_{\max} parameter.

The two shape parameters measured in this work were compared with model predictions and found to be compatible with most mass composition scenarios at the two sigma level. However, different hadronic models predict shape parameters which span different regions in the (R, L) plane, even when considering all possible mass compositions. Therefore, a future measurement of the average longitudinal profile shape with smaller systematic uncertainties could provide constraints on high-energy interaction models.

Acknowledgments

The successful installation, commissioning, and operation of the Pierre Auger Observatory would not have been possible without the strong commitment and effort from the technical and administrative staff in Malargüe. We are very grateful to the following agencies and organizations for financial support:

Argentina – Comisión Nacional de Energía Atómica; Agencia Nacional de Promoción Científica y Tecnológica (ANPCyT); Consejo Nacional de Investigaciones Científicas y Técnicas (CONICET); Gobierno de la Provincia de Mendoza; Municipalidad de Malargüe; NDM Holdings and Valle Las Leñas; in gratitude for their continuing cooperation over land access; Australia – the Australian Research Council; Brazil – Conselho Nacional de Desenvolvimento Científico e Tecnológico (CNPq); Financiadora de Estudos e Projetos (FINEP); Fundação de Amparo à Pesquisa do Estado de Rio de Janeiro (FAPERJ); São Paulo Research Foundation (FAPESP) Grants No. 2010/07359-6 and No. 1999/05404-3; Ministério da Ciência, Tecnologia, Inovações e Comunicações (MCTIC); Czech Republic – Grant No. MSMT CR LTT18004, LO1305, LM2015038 and CZ.02.1.01/0.0/0.0/16_013/0001402; France – Centre de Calcul IN2P3/CNRS; Centre National de la Recherche Scientifique (CNRS); Conseil Régional Ile-de-France; Département Physique Nucléaire et Corpusculaire (PNC-IN2P3/CNRS); Département Sciences de l’Univers (SDU-INSU/CNRS); Institut Lagrange de Paris (ILP) Grant No. LABEX ANR-10-LABX-63 within the Investissements d’Avenir Programme Grant No. ANR-11-IDEX-0004-02; Germany – Bundesministerium für Bildung und Forschung (BMBF); Deutsche Forschungsgemeinschaft (DFG); Finanzministerium Baden-Württemberg; Helmholtz Alliance for Astroparticle Physics (HAP); Helmholtz-Gemeinschaft Deutscher Forschungszentren (HGF); Ministerium für Innovation, Wissenschaft und Forschung des Landes Nordrhein-Westfalen; Ministerium für Wissenschaft, Forschung und Kunst des Landes Baden-Württemberg; Italy – Istituto Nazionale di Fisica Nucleare (INFN); Istituto Nazionale di Astrofisica (INAF); Ministero dell’Istruzione, dell’Università e della Ricerca (MIUR); CETEMPS Center of Excellence; Ministero degli Affari Esteri (MAE); México – Consejo Nacional de Ciencia y Tecnología (CONACYT) No. 167733; Universidad Nacional Autónoma de México (UNAM); PAPIIT DGAPA-UNAM; The Netherlands – Ministry of Education, Culture and Science; Netherlands Organisation for Scientific Research (NWO); Dutch national e-infrastructure with the support of SURF Cooperative; Poland – National Centre for Research and Development, Grant No. ERA-NET-ASPERA/02/11; National Science Centre, Grants No. 2013/08/M/ST9/00322, No. 2016/23/B/ST9/01635 and No. HARMONIA 5-2013/10/M/ST9/00062, UMO-2016/22/M/ST9/00198; Portugal – Portuguese national funds and FEDER funds within Programa Operacional Factores de Competitividade through Fundação para a Ciência e a Tecnologia (COMPETE); Romania – Romanian Ministry of Research and Innovation CNCS/CCCDI-UESFISCDI, projects PN-III-P1-1.2-PCCDI-2017-0839/19PCCDI/2018, PN-III-P2-2.1-PED-2016-1922, PN-III-P2-2.1-PED-2016-1659 and PN18090102 within PNCDI III; Slovenia – Slovenian Research Agency; Spain – Comunidad de Madrid; Fondo Europeo de Desarrollo Regional (FEDER) funds; Ministerio de Economía y Competitividad; Xunta de Galicia; European Community 7th Framework Program Grant No. FP7-PEOPLE-2012-IEF-328826; USA – Department of Energy, Contracts No. DE-AC02-07CH11359, No. DE-FR02-04ER41300, No. DE-FG02-99ER41107 and No. DE-SC0011689; National Science Foundation, Grant No. 0450696; The Grainger Foundation; Marie Curie-IRSES/EPLANET; European Particle Physics Latin American Network; European Union 7th Framework Program, Grant No. PIRSES-2009-GA-246806; and

UNESCO.

References

- [1] Pierre Auger Collaboration, A. Aab *et al.*, *Nucl. Instrum. Meth. A*, **798** (2015) 172-213, [[arXiv:1502.01323](#)].
- [2] Pierre Auger Collaboration, P. Abreu *et al.*, *Astropart. Phys.* **35** (2012) 591–607, [[arXiv:1201.2276](#)].
- [3] M. Unger *et al.*, *Nucl. Instrum. Meth. A* **588** (2008) 433, [[arXiv:0801.4309](#)].
- [4] T.K. Gaisser and A.M. Hillas, *Proc. 15th ICRC, Plovdiv, Bulgaria* **8** (1977) 353.
- [5] M. Ave *et al.*, *Astropart. Phys.* **42** (2013) 90.
- [6] S. Andringa, R. Conceição and M. Pimenta, *Astropart. Phys.* **34** (2011) 360–367.
- [7] J.A.J. Matthews *et al.*, *J. Phys. G* **37** (2010) 025202, [[arXiv:0909.4014](#)].
- [8] The HiRes/MIA Collaboration, T. Abu-Zayyad *et al.*, *Astropart. Phys.* **16** (2001) 1–11.
- [9] G. Hughes for the High Resolution Fly’s Eye Collaboration, *Proc. 30th ICRC, Merida, Mexico* **4** (2007) 405–408.
- [10] R. Conceição *et al.*, *24th European Cosmic Ray Symposium*, *J. Phys. Conf. Ser.* **632** (2015) no.1, 012087.
- [11] Pierre Auger Collaboration, A. Aab *et al.*, *Phys. Rev. D* **90** (2014) 122005.
- [12] Pierre Auger Collaboration, J. Abraham *et al.*, *Astropart. Phys.* **33** (2010) 108–129, [[arXiv:1002.0366](#)].
- [13] B. Fick *et. al.*, *JINST* **1** (2006) P11003.
- [14] Pierre Auger Collaboration, P. Abreu *et al.*, *JINST* **8** (2013) P04009, [[arXiv:1303.5576](#)].
- [15] V. Verzi for the Pierre Auger Collaboration, *Proc. 33rd ICRC, Rio de Janeiro, Brazil* (2013), [[arXiv:1307.5059](#)].
- [16] D. Heck *et al.*, *Report FZKA 6019* **26** (1998).
- [17] T. Pierog and K. Werner, *Phys. Rev. Lett.* **101** (2008) 171101.
- [18] S. Ostapchenko, *Phys. Rev. D* **83** (2011) 014018.
- [19] F. Riehn *et al.*, *PoS(ICRC2017)* **301** (2017) [[arXiv:1709.07227](#)].